Arctic mixed-phase clouds in large-eddy simulations and a mixed-layer model

Xiyue Zhang[1], **Tapio Schneider**[1], **and Colleen M. Kaul** [1]

[1]Environmental Science and Engineering, California Institute of Technology, Pasadena, California, USA.

Key Points:

- Large-eddy simulations of Arctic mixed-phase stratocumulus clouds are compared with ISDAC observations
- Sensitivities of the Arctic boundary layer to temperature, inversion strength, and humidity are explored through LES
- Mixed-layer theory explains most of the sensitivities, with minor discrepancies resulting from microphysical effects

Corresponding author: X. Zhang, xiyue@caltech.edu

Abstract

The stable and cloudy Arctic boundary layer (BL) is an essential component of the Arctic climate system and is often thought to contribute to Arctic amplification of global warming. However, regional and global climate models that depend on parameterized representations of BL turbulence and clouds show large uncertainties in simulated Arctic cloudiness. We use large-eddy simulations (LES) that explicitly resolve BL turbulence and clouds to explore the sensitivities of Arctic BL clouds to idealized climate change. Simulated liquid water path is found to increase with BL temperature and free-tropospheric relative humidity, but it decreases with inversion strength across the BL top. The trends shown by the LES climate change experiments can be largely reproduced by a mixed-layer model that excludes microphysical processes, except for a few LES cases when ice-phase microphysical processes lead to BL decoupling. Thus, these results offer encouragement that analysis methods used to explain the sensitivities of lower-latitude BL clouds to climate change can be usefully extended to an important category of Arctic BL clouds.

1 Introduction

The Arctic boundary layer (BL) is known for its ubiquitous temperature inversion and mixed-phase clouds. Though the inversion strength and height vary from season to season, the overall inversion probability is as high as 90% [*Tjernström and Graversen*, 2009]. Annual-mean cloud fraction is around 70%, with a maximum greater than 80% in autumn [*Wang and Key*, 2005; *Kay and L'Ecuyer*, 2013]. These characteristics have manifold impacts on high-latitude climate. For example, Arctic clouds warm the surface in all seasons but summer because their longwave greenhouse effect predominates over shortwave effects, unlike for their subtropical counterparts [*Intrieri et al.*, 2002; *Kay and L'Ecuyer*, 2013]. Therefore, Arctic cloud feedbacks may operate differently from those at lower latitudes. Moreover, anomalous spring-time clouds have been postulated to influence the autumn sea ice minimum through long-term effects on the surface energy balance [*Cox et al.*, 2016].

Climate change in the polar regions has interested scientists ever since the first modeling studies of increased CO_2 concentration. Arctic amplification of surface warming is a robust feature in climate models under greenhouse warming [*Manabe and Wetherald*, 1975; *Holland and Bitz*, 2003]. In the recent decades, the Arctic has been experiencing rapid changes. The Arctic sea ice extent, most prominently in September, has shown accelerated loss since the beginning of the modern satellite record [*Stroeve et al.*, 2012]. Amplified warming in high northern latitudes has also been observed over the past decades, especially in winter [*Schneider and Held*, 2001], and it has been observed to be surface intensified, trends that can be discerned in observational records despite the large internal variability in high latitudes [*Serreze et al.*, 2009]. Furthermore, significant increases in specific humidity have been observed, but relative humidity changes are more complex [*Sherwood et al.*, 2010; *Serreze et al.*, 2012]. Cloud feedbacks and the trapping of heat under the stable inversion are thought to contribute to Arctic amplification of global warming [*Wetherald and Manabe*, 1975; *Holland and Bitz*, 2003; *Graversen and Wang*, 2009]. However, the sign of any cloud feedback in high latitudes is uncertain [*Kay et al.*, 2016]. In GCMs, low clouds depends on parameterized turbulence and convection which are developed mainly for the lower latitudes. In fact, the GCMs show large spread in simulated seasonal cycle of Arctic cloud fraction [*Karlsson and Svensson*, 2013]. A key step towards constraining Arctic cloud feedbacks is to project how the clouds respond to changes of temperature, inversion strength, and moisture content of the free troposphere, without the dependence on parameterizations.

Recent modeling studies have focused on microphysical and dynamical processes maintaining Arctic mixed-phase stratocumulus clouds. *Savre et al.* [2014] investigated how the persistence of Arctic mixed-phase clouds depends on microphysical processes and moisture sources in the sub-cloud layer and in the free troposphere. They found that microphysical processes (ice sublimation) play an important role in controlling the BL structure. A more idealized study by *Solomon et al.* [2014] found a similar role for ice microphysics in controlling BL moisture. One important question that was not addressed by either study is how Arctic mixed-phase clouds respond to climate change. Will the clouds become more persistent or will they more easily dissipate as the Arctic warms?

Here we use large-eddy simulations (LES) with the recently developed Python Cloud Large Eddy Simulation code (PyCLES) [*Pressel et al.*, 2015] to investigate systematically the response of Arctic BL clouds to different kinds of idealized changes. We base our study on the Indirect and Semi-direct Aerosol Campaign (ISDAC) LES intercomparison study [*Ovchinnikov et al.*, 2014]. In an idealized setup (hereafter ISDAC_i) mimicking conditions during the ISDAC observational campaign, we investigate the sensitivities of Arctic mixed-phase stratocumulus clouds to temperature, cloud-top inversion strength, and free-tropospheric moisture. This is a first step toward understanding how Arctic low clouds respond to climate change. We then use a mixed-layer model (MLM) to elucidate the cloud response to perturbations seen in the LES. MLMs have been extensively used to study stratocumulus-topped BLs over subtropical oceans [*Lilly*, 1968; *Bretherton and Wyant*, 1997; *Gesso et al.*, 2014; *De Roode et al.*, 2014],

but rarely Arctic BL clouds. Yet they turn out to be similarly useful for providing insight into controls of Arctic stratocumulus clouds.

We begin by comparing our LES and its one-moment mixed-phase microphysics scheme with the ISDAC LES intercomparison study and observations. Then we describe the idealized ISDAC_i setup and the climate change experiments. Next, we introduce the MLM, compare it with the LES results, and discuss how parameters in the MLM govern the BL and cloud structure in ISDAC_i.

2 Large-Eddy Simulation Model

2.1 LES Code

We work with the recently developed PyCLES code, which uses total water specific humidity and specific entropy as prognostic variables to solve the anelastic equations of motion [*Pressel et al.*, 2015]. PyCLES has been used successfully to simulate subtropical marine BL clouds [*Tan et al.*, 2016, 2017; *Pressel et al.*, 2017]. This is its first application in a polar setting.

We use a nominally 5th-order Weighted Essentially Non-Oscillatory (WENO5) advection scheme for momentum and scalars, and a strong stability preserving 3rd-order, 3-stage Runge-Kutta method for time-stepping. The time-steps are adaptive with a target Courant number of 0.7. The numerical dissipation implicit in the WENO scheme is used in lieu of an explicit subgrid-scale dissipation scheme, as this has been found to lead to the most faithful simulation of subtropical stratocumulus [*Pressel et al.*, 2017]. We only use a Smagorinsky-Lilly subgrid-scale closure near the surface to transfer momentum between the LES domain and the surface. Monin-Obukhov similarity theory is used to compute the surface flux of momentum at the lower boundary conditions. The roughness length is set to 4×10^{-4} m. The surface sensible and latent heat fluxes are zero for all simulations presented in this study. The grid resolution is 50 m in the horizontal, with doubly periodic boundary conditions, and 10 m in the vertical. The computational domain extends 3.2 km $\times$ 3.2 km in the horizontal and is 2.56 km deep in the vertical.

2.2 Microphysics

The modeling of mixed-phase microphysics remains an active area of research. We use a relatively simple one-moment microphysics scheme that captures basic features of Arctic mixed-phase clouds [*Kaul et al.*, 2015]. Cloud condensates are diagnosed using an empirical partition function $f(T)$ that models the liquid fraction λ of the condensate as a function of temperature [*Grabowski*, 1998; *Kaul et al.*, 2015; *Pressel et al.*, 2015],

$$\lambda(T) = \begin{cases} 0 & \text{for } T < T_i, \\ f(T) & \text{for } T_i \leq T \leq T_f, \\ 1 & \text{for } T_f < T, \end{cases} \tag{1}$$

where $T_f = 273.15$ K is the freezing point, $T_i \approx 235$ K is the homogeneous nucleation temperature. The partition function $f(T)$ is a based on CALIPSO observations of fraction of supercooled water clouds [*Hu et al.*, 2010],

$$f(T) = \frac{1}{\left[1 + e^{-k(T - T_{\mathrm{lf}})}\right]^3}. \tag{2}$$

The coefficients $k = 0.33$ K^{-1} and $T_{\mathrm{lf}} = 241.9$ K in (2) are chosen so that our partition function (2) provides an accurate least-squares fit to the data and equations (1) and (2) in *Hu et al.* [2010]. This functional form differs from the one used in *Kaul et al.* [2015], with (2) producing less liquid between 235 K and 253 K, but slightly more liquid above 253 K (Figure 1). Although liquid fraction close to 100% at 240–250 K was observed in Arctic low clouds

[*de Boer et al.*, 2009], we choose a function that is more general and representative of the global liquid fraction.

The same partition function (1) is used to determine the effective specific latent heat L in the mixed phase and a thermodynamically consistent saturation vapor pressure [*Pressel et al.*, 2015]. Precipitation species (rain and snow) are prognostic. The processes that govern the transformation between species include autoconversion, aggregation, and phase changes. Sedimentation of cloud condensate is not taken into account. The scheme uses exponential particle size distribution functions for rain, ice, and snow. Cloud ice has a constant intercept parameter $N_{0,\text{ice}} = 1 \times 10^7 \ \text{m}^{-4}$. The snow intercept parameter $N_{0,\text{snow}}$ is a diagnostic function of snow specific humidity [*Morrison et al.*, 2011]. More details of the scheme are given in *Kaul et al.* [2015].

We made several minor modifications to the microphysical source terms in *Kaul et al.* [2015]. The thermodynamic variable G, which represents the vapor diffusion of an ice-water sphere and determines the mass growth rate of liquid droplets or ice crystals, is taken without approximation, following *Straka* [2009], as

$$G(T,P) = \left[\frac{\rho_{l/i} R_v T}{D p_v^*(T)} + \left(\frac{L}{R_v T} - 1\right)\frac{L\rho_{l/i}}{\kappa T}\right]^{-1}.$$

Here, $\rho_{l/i}$ is the density of liquid or ice, depending on the process, L is the effective latent heat, and p_v^* is the saturation vapor pressure; D is the water vapor diffusivity, which increases with temperature and decreases with pressure; and κ is the thermal conductivity, which depends approximately linearly on temperature. The detailed formulations of D and κ are given in *Straka* [2009]. The function G increases approximately exponentially with temperature and is used in formation (autoconversion), evaporation, and deposition/sublimation of droplets and ice crystals.

The formation of precipitation and evaporation/sublimation of hydrometeors contribute to the entropy tendency. The small heat transfer and the aerodynamic drag during sedimentation are also included in the entropy source/sink terms, as specified in *Pressel et al.* [2015].

2.3 Radiative Transfer

The default ISDAC longwave radiation scheme is idealized and depends solely on cloud liquid water content [*Ovchinnikov et al.*, 2014]. In order to capture radiative flux changes under climate change, we use the RRTMG [*Iacono et al.*, 2008] integrated into PyCLES. Additional information on temperature, humidity, and ozone above the LES domain is required to calculate radiative fluxes. Therefore, the standard atmospheric profiles from the Mixed-Phase Arctic Cloud Experiment (M-PACE) LES intercomparision project are patched to the ISDAC temperature and humidity profiles. RRTMG produces a more realistic radiative flux profile, which results in slightly warmer BL compared to the ISDAC simulations with idealized radiation. RRTMG is called every 60 simulated seconds in PyCLES.

The liquid effective radius uses the parameterization by *Martin et al.* [1994] for warm stratocumulus clouds [*Blossey et al.*, 2013; *Tan et al.*, 2016]. The mean ice effective radius follows an empirical relation that depends on temperature and ice water content [*Boudala et al.*, 2002],

$$r_{e,ice} = 34.419 \ \mu\text{m} \times \left(\frac{\text{IWC}}{1 \ \text{g m}^{-3}}\right)^{0.06} \exp\left[0.013 \ \text{K}^{-1}(T - 273.15 \ \text{K})\right],$$

where IWC is the ice water concentration (units of g m^{-3}). The mean ice effective radius is mainly a function of temperature and increases with temperature at a rate of $\sim 0.5 \ \mu\text{m K}^{-1}$. It is only sensitive to IWC at low IWC values [*Boudala et al.*, 2002]. Only cloud ice is included in the radiative transfer calculation. The ice effect on cloud infrared optical depth is minimal because the cloud layer is dominated by the optically thick liquid water.

3 ISDAC Comparison

3.1 Case Description and Setup

The ISDAC LES intercomparison is based on observations of a long-lived mixed-phase cloud on April 26, 2008 north of Barrow, Alaska [*Ovchinnikov et al.*, 2014]. Soundings at Barrow show a stable surface layer below a well-mixed cloud layer. The boundary layer is capped by a strong potential temperature inversion, with a dry free atmosphere above.

Our setup generally follows the ISDAC LES intercomparison. We define θ_{li} following *Tripoli and Cotton* [1981] and *Pressel et al.* [2015], as

$$\theta_{li} = \theta \exp\left(-\frac{L}{Tc_p}\frac{q_l + q_i}{1 - q_t}\right), \tag{3}$$

where the effective specific latent heat L is a weighted sum of that for vaporization and sublimation, using the partitioning function (1) as weight. Surface heat fluxes are set to zero because the fluxes over sea ice were negligible during the field campaign [*Ovchinnikov et al.*, 2014]. Large-scale subsidence is specified to be linear with height below the initial inversion at 825 m altitude, and is constant with height above:

$$w_{LS} = \begin{cases} -5 \times 10^{-6}\ \mathrm{s}^{-1} \cdot z, & z < 825\ \mathrm{m}, \\ -4.125 \times 10^{-3}\ \mathrm{m\ s}^{-1}, & z \geq 825\ \mathrm{m}. \end{cases} \tag{4}$$

The choice of the subsidence profile is justified in *Ovchinnikov et al.* [2014], and it is kept fixed for all simulations here. In addition to the large-scale subsidence, relaxation of the prognostic variables above 1200 m altitude toward the initial conditions is also included. Relaxation is specified as an additional source term in the prognostic equations. We relax specific entropy s (a native PyCLES variable instead of the otherwise common liquid-ice potential temperature) and total water specific humidity q_t toward the initial profiles above 1200 m, with a relaxation timescale of 1 hour. Horizontal velocities are relaxed toward the initial profiles throughout the domain with a timescale of 2 hours. The simulation was run for 8 hours.

3.2 Comparison with LES Intercomparison Results

Figure 2 shows the domain-mean profiles of liquid-ice potential temperature θ_{li}, total-water specific humiditiy q_t, liquid-water specific humidity q_l, ice specific humidity q_i, and snow specific humidity q_{snow}, all averaged over the last hour of the simulation. Observations gathered by the National Research Council of Canada Convair-580 aircraft from ISDAC flight 31 are also shown for comparison [*McFarquhar et al.*, 2011]. As in the simulations in the ISDAC LES intercomparison study, the BL in our simulation becomes well mixed as turbulence generated by cloud-top radiative cooling mixes the cloud and sub-cloud layer. The initially stable layer near the surface is not maintained in our simulations; cloud-top radiative cooling leads to a BL that is cooler than was observed. A mixed-phase cloud layer of $\sim$300 m thickness persists throughout the simulation (Figure 3a). Simulated cloud liquid water is generally higher than observed, mainly because of the deviations of θ_{li} and q_t from the observed values. These differences arise because the idealized initial profiles were based on a sounding at Barrow, Alaska, about 120 km south of the site of the aircraft observations. The biases in the simulations can be reduced if large-scale forcing fields are included to maintain the θ_{li} profile closer to the initial conditions. The observed ice water specific humidity q_i, which includes cloud ice and snow (observations cannot distinguish cloud ice from snow), shows large variance but is generally higher than in the LES simulation. Models with more complex microphysics schemes still tend to underestimate q_i [*Ovchinnikov et al.*, 2014]. Thus, if this bias arises from microphysical processes, it suggests that models more generally may be missing potentially important ice microphysical processes.

Liquid water path (LWP) at the end of the eighth hour in our simulation is $45.5\ \mathrm{g\ m}^{-2}$, which is within the range of the intercomparison values (Figure 3b). Without ice microphysics,

LWP is about $47\ \mathrm{g\ m^{-2}}$. The sum of ice water path (IWP) and snow water path (SWP) is below the intercomparison value [*Ovchinnikov et al.*, 2014]. However, given our relatively simple treatment of microphysics, our LES captures the main features of the BL during ISDAC as well as other LES in the intercomparison.

3.3 Sensitivity Tests

To check for convergence of the simulations, we ran the ISDAC case with increased domain size and reduced horizontal grid spacing. Doubling the domain size and/or the horizontal resolution (halving the grid spacing) produced no significant changes to the results (not shown, in agreement with *Kaul et al.*, 2015).

4 ISDAC_i: Idealized Climate Change

4.1 Setup

Given that the initially decoupled surface layer becomes well-mixed in the ISDAC simulations (Figure 2), we initialize with well-mixed profiles of θ_{li} and q_t below the inversion at height z_i:

$$\theta_{li} = \begin{cases} \theta_{li,0}, & z \le z_i \\ \theta_{li,0} + \Delta\theta_{li} + \Gamma_\theta (z - z_i), & z > z_i \end{cases}$$

$$q_t = \begin{cases} q_{t,0}, & z \le z_i, \\ q_s(T)\mathcal{H}_f, & z > z_i. \end{cases}$$

Here, $q_{t,0} = q_s(T_0)\mathcal{H}_0$, where q_s is the saturation specific humidity, T_0 is the surface temperature, and $\mathcal{H}_0 = 0.8$ is a near-surface relative humidity. We assume a constant θ gradient Γ_θ and relative humidity $\mathcal{H}_f$ above the cloud top. The variables are listed in Table 1. This setup enables us to explore different initial conditions that help us to gain insight into climate change in polar regions.

Idealized climate change studies are conducted by varying three variables (Table 2): (1) The initial mixed-layer liquid-ice potential temperature $\theta_{li,0}$. Changing $\theta_{li,0}$ warms or cools the entire atmospheric column. (2) The inversion strength $\Delta\theta_{li}$. Changing $\Delta\theta_{li}$ can be thought of as changing the horizontal advection in the free troposphere from lower latitudes, or as changing the degree to which warming is surface amplified. The inversion strength directly affects entrainment processes at the cloud top and the amount of free-tropospheric moisture. (3) The relative humidity $\mathcal{H}_f$ in the free troposphere. Changing $\mathcal{H}_f$ can be thought of as altering the moisture content of air masses advected from lower latitudes.

We ran 64 simulations with different initial conditions, each for 12 hours. Due to the setup, there is no surface heat flux to balance cloud top entrainment. Most simulations cannot reach steady state in the time scale we consider here. Therefore, we analyze both the end states and the time tendencies of the BL sensitivities.

4.2 Results

We first show simulations where only one of the variables in Table 2 is varied at a time. Figures 5 and 6 show the domain mean profiles averaged over the 12th hour and the domain mean time evolution of these experiments. The BL becomes well-mixed in all simulations, except in some experiments when $\mathcal{H}_f$ is varied.

- Warming the entire column by increasing $\theta_{li,0}$ results in different q_t profiles, with larger specific humidity jumps above the cloud top (Figure 5b), and vice versa for cooling the entire column. The sensitivities of q_l and q_i to warming have opposite signs (Figure 5c, d), because the liquid fraction increases with temperature. Despite a decrease of q_i with

234 **Table 1.** List of variables

Variable	Unit	Description	Baseline value
z_i	m	Cloud top height	820 m
z_b	m	Cloud base height	-
θ_{li}	K	Liquid-ice potential temperature	-
$\theta_{li,0}$	K	**Liquid-ice potential temperature at the surface**	265 K
$\Delta\theta_{li}$	K	**Inversion strength at cloud top**	5 K
q_t	kg kg^{-1}	Total water specific humidity	-
$q_{t,0}$	kg kg^{-1}	Total water specific humidity at the surface	1.5×10^{-3} kg kg^{-1}
$q_s(T)$	kg kg^{-1}	Saturation specific humidity at temperature T	-
$\mathcal{H}_0$	-	Relative humidity at the surface	80%
$\mathcal{H}_f$	-	**Free-tropospheric relative humidity**	60%
Γ_θ	K km^{-1}	Free-tropospheric θ lapse rate	5 K km^{-1}
w_e	m s^{-1}	Entrainment rate	-
a_1, a_2	-	Convective entrainment coefficients	-
Ri	-	Richardson number	-
w_*	m s^{-1}	Generalized convective velocity	-
ΔF_R	W m^{-2}	Radiative flux jump	-
$\Delta\theta_l$	K	Inversion strength in the mixed-layer model	-
$\Delta\theta_v$	K	Inversion strength in virtual potential temperature	-
ρ_0	kg m^{-3}	Air density	-
c_p	J K^{-1} kg^{-1}	Specific heat of air at constant pressure	1004 J K^{-1} kg^{-1}
B	m^2 s^{-3}	BL-mean buoyancy flux	-
T_0	K	Surface temperature	265 K
T_{LCL}	K	Temperature at lifting condensation level or cloud base	-

[a] Variables in bold are varied in the idealized climate change experiments.

Table 2. List of parameters and ranges over which they are varied in the sensitivity studies with ISDAC_i. Baseline parameter values in bold.

Variable	Range
$\theta_{li,0}$	261, **265**, 269, 273 K
$\Delta\theta_l$	3, **5**, 7, 9 K
$\mathcal{H}_f$	50, **60**, 70, 80%

warming, $q_{\rm snow}$ is less sensitive, because snow also forms by aggregating with cloud liquid. The cloud top height z_i increases moderately with temperature, resulting in an upward shift of the cloud layer (Figure 6a). The cloud thickness remains insensitive to warming (Figure 6c), yet the LWP increases (Figure 6b). The higher temperatures also allow rain formation and snow melt.

- Increasing the inversion strength $\Delta\theta_{li}$ significantly decreases the BL height (Figure 5e–h). At the same time, the specific humidity in the free troposphere increases with inversion strength because of the free-tropospheric temperature increase, thus reducing the BL drying through cloud-top entrainment. The change in Δq_t outweighs the change in w_e, resulting in higher q_t in the BL as $\Delta\theta_{li}$ increases. The cloud layer thins (Figure 6c) and LWP decreases (Figure 6b) as $\Delta\theta_{li}$ strengthens.
- Increasing the relative humidity $\mathcal{H}_f$ in the free troposphere has little impact on θ_{li} (Figure 5i), but it substantially moistens the BL (Figure 5j). This is mainly achieved by reduced entrainment drying at the cloud top: the free troposphere moistens while the entrainment rate stays relatively constant. The cloud base height decreases slightly with increasing $\mathcal{H}_f$ (Figure 5i), leading to a thicker cloud and higher LWP (Figure 6b, c).

When more than one parameter is varied at a time, a combination of the changes described above occurs. The BL height and LWP at the end of the simulations are shown in Figure 7a and b, in the slice of parameter space spanned by variations in inversion strength $\Delta\theta_{li}$ and specific humidity above the cloud top q_t^+. The BL height varies primarily with $\Delta\theta_{li}$, while the LWP varies primarily with q_t^+. To understand these results quantitatively, we turn to the MLM, which may be expected to yield insight for the simulations we conducted.

5 Mixed-layer Model

5.1 Model Description

In order to analyze the ISDAC_i cases, we use a MLM with θ_l, q_t, and z_i as prognostic variables [*Lilly*, 1968; *Bretherton and Wyant*, 1997; *Gesso et al.*, 2014]:

$$\frac{dz_i}{dt} = w_e + w_{LS}(z_i), \tag{5}$$

$$\frac{d\theta_l}{dt} = \frac{1}{z_i}\left(w_e\Delta\theta_l - \frac{\Delta F_R}{\rho c_p}\right), \tag{6}$$

$$\frac{dq_t}{dt} = \frac{1}{z_i}w_e\Delta q_t. \tag{7}$$

Here, $w_{LS}(z)$ is the large-scale subsidence rate in (4). (See Table 1 for a list of variables.) Microphysical and ice processes are not included in the MLM. Therefore, θ_l in the MLM is defined by setting $q_i = 0$ and $L = L_v$ in (3), and we interpret it as representing θ_{li} in the LES. A standard saturation adjustment procedure is called to get the liquid water specific humidity at every time step, which is then used for radiative transfer calculations. Time-stepping uses a 2nd-order 2-stage Runge-Kutta method with fixed time steps of 10 s. Radiative transfer uses the same RRTMG scheme as PyCLES and is called at every time step. The initial conditions

are identical to those in the LES. After the BL values are solved at each time step, vertical profiles are created using the initial free tropospheric conditions. The MLM vertical resolution is 2 m.

An entrainment rate formula is needed to close the set of MLM equations. We parameterize the entrainment rate following *Moeng et al.* [1999] as

$$w_e = a_1 \frac{w_*}{\mathrm{Ri}} + \frac{\Delta F_R}{\rho_0 c_p \Delta\theta_l},$$

where we assumed that $\Delta\theta_l \approx \Delta\theta_v$ and that the longwave radiative flux jumps nearly discontinuously by ΔF_R at the cloud-topped BL, driving radiative cooling at the top and with it the mixed-layer turbulence. With the convective Richardson number $\mathrm{Ri} = g\Delta\theta_l z_i/(\theta_v w_*^2)$ and the mixed-layer scaling for the mean buoyancy flux $B \propto w_*^3/z_i$, the entrainment rate w_e can be alternatively written as

$$w_e = a_2 \frac{B}{\Delta\theta_l} + \frac{\Delta F_R}{\rho_0 c_p \Delta\theta_l}. \tag{8}$$

The first term on the right-hand side is a convective term that represents entrainment owing to turbulent fluxes at the BL top. The second term represents the radiative flux jump at the cloud top. Both terms arise in an integration of the buoyancy budget across the BL top [*Moeng et al.*, 1999; *Stevens*, 2006]. The jumps ΔF_R, $\Delta\theta_l$, and Δq_t represent jumps across the entrainment zone. In the LES, we diagnose the jumps as the differences between z_i and $1.05z_i$ [*Moeng et al.*, 1999]. In the MLM, we determine the jumps $\Delta\theta_l$ and Δq_t analogously. But because the radiative flux profile is relatively smooth at the entrainment zone, ΔF_R determined in this way is sensitive to the MLM vertical resolution. Therefore, we define ΔF_R to be half the total radiative flux jump across the BL top. This minimizes the resolution dependence of ΔF_R, and enables reliable representation of the radiative flux jump across the entrainment zone.

Because the BL mean buoyancy flux B cannot be obtained directly from the MLM, we parameterize it based on LES results. The lack of surface fluxes in our setup makes the usual assumption of the flux varying linearly with height inapplicable. The diagnosed B across 64 ISDAC_i LES simulations has a mean value of 6.34×10^{-3} m^2 s^{-3} and a standard deviation of 2.6×10^{-3}m^2 s^{-3}. We simply assume B to be a constant parameter, which still leads to reasonable entrainment rates obtained with the formulation (8).

Figure 8 shows the entrainment rates diagnosed from the ISDAC_i LES runs and parameterized according to (8). The entrainment rate w_e is diagnosed using (5), where dz_i/dt is approximated by the change of cloud top height over the last 4 hours of the simulations, and $w_{LS}(z_i)$ is the subsidence rate at the cloud top level. The convective entrainment coefficient $a_2 = 2.0$ is taken from a linear fit of the right-hand side of (8) to w_e diagnosed from the 64 ISDAC_i LES simulations. The parameterized entrainment rates lie close to the 1:1 line, with some scatter. In most cases, the convective term (Term 1) dominates over the radiative term (Term 2), which is more likely at higher entrainment rates. Note that the empirical coefficients used here are not necessarily representative of the entire Arctic region but may be specific to the cases investigated here.

5.2 Comparison with LES

Figure 9 and 10 show the profiles and timeseries of the MLM simulations, which are to be compared with the LES in Figures 5 and 6. The profiles of θ_l and q_t agree well with the LES results when temperature or inversion strength are varied. The MLM also shows qualitative agreement in cloud top height sensitivities to temperature and inversion strength. The closeness of the q_l profiles between MLM and LES results are particularly encouraging (compare Figure 5c, g and Figure 9b, e), especially given that microphysical processes are not represented in the MLM. When only $\mathcal{H}_f$ is varied, q_l shows greater variations in MLM than in LES. For larger free-tropospheric relative humidity $\mathcal{H}_f$, microphysical processes become important in the LES, which will be discussed later.

When plotted in $\Delta\theta_l$–q_t^+ space, the BL height and LWP show similar sensitivities in the LES and MLM. Both LES and MLM show the expected decrease in inversion height z_i with inversion strength (Figure 7a and c), because a stronger inversion implies reduced entrainment (8), which in turn implies a reduced z_i according to the MLM mass balance (5). There is a general a decrease of LWP with $\Delta\theta_l$ and increase with q_t^+, for both LES and MLM (Figure 7b and d).

Some differences between the LWP patterns can be attributed to decoupled BLs at large $\Delta\theta_l$ and q_t^+ simulated by LES. To diagnose decoupling, we use the buoyancy integral ratio (BIR) [*Turton and Nicholls*, 1987; *Bretherton and Wyant*, 1997],

$$\mathrm{BIR} = -\frac{\int_{z<z_b,\langle w'\theta_v'\rangle<0}\langle w'\theta_v'\rangle\, dz}{\int_{z>z_b,\langle w'\theta_v'\rangle>0}\langle w'\theta_v'\rangle\, dz}.$$

The angle brackets denote a horizontal average. We choose $\mathrm{BIR} = 1.5$ to be the threshold value above which the BL is consider decoupled [*Savre et al.*, 2014]. The dynamics of the BL is no longer representable by the MLM when the mixed-layer assumption breaks down.

Furthermore, the two models cover slightly different parts of the parameter space for the same 64 cases. The LES simulations have a systematic shift towards higher inversion strength from the initial conditions, While the MLM simulations tend to preserve the initial inversion strength, this is not the case for LES. Weaker inversions ($\Delta\theta_l$ = 3 K, 5 K) are strengthened, and stronger inversions ($\Delta\theta_l$ = 9 K) are weakened at the end of LES simulations. These differences arise for mainly two reasons: 1) motions above the mixed-layer are not represented in MLM, but in LES the lapse rate right above the cloud top is smoothed due to mixing; 2) cloud top radiative cooling is approximated by the difference of radiative flux at two levels.

5.3 Parameter Dependencies of LWP

The LWP pattern from the MLM seems non-monotonic when plotted in the $\Delta\theta_l$–q_t^+ plane (Figure 7b). However, three parameters— $\theta_{l,0}$, $\Delta\theta_l$, and $\mathcal{H}_f$—were varied to produce this set of simulations. If we stratify the simulations for constant $\mathcal{H}_f$ (Figure 11), LWP changes monotonically with $\Delta\theta_l$ and q_t^+. LWP can be approximated by assuming an adiabatic liquid water lapse rate Γ_l that is constant with height, leading to $\mathrm{LWP} \propto \Delta z_{\mathrm{cloud}}^2 \Gamma_l$. Here, $\Delta z_{\mathrm{cloud}}$ is cloud thickness, which equals the difference between cloud top height z_i and the cloud base height z_b.

Due to the lack of surface fluxes, most simulations do not reach equilibrium at the end of the 12th hour, making it difficult to interpret the results using steady-state solutions of the MLM. However, a strong positive correlation among cases is found between $\Delta z_{\mathrm{cloud}}$ at the end of the simulations and its time tendency $d\Delta z_{\mathrm{cloud}}/dt$ (Figure A.1). The same is true for z_i, because all simulations have the same initial cloud top height (for more details, see Appendix A). These correlations make it possible to analyze the cloud properties using the time tendency terms from the MLM.

In order to understand how cloud thickness changes, it is necessary to know what governs the changes of z_b, an understanding of which can be derived in the MLM framework. We start by defining

$$z_b = \frac{1}{\Gamma_d}\left(T_0 - T_{\mathrm{LCL}}\right),$$

where Γ_d is the dry adiabatic lapse rate, and T_{LCL} is the lifting condensation level temperature located at z_b. To compare the rate of change of z_b to the mass balance (5), we differentiate

$$\frac{dz_b}{dt} = \frac{1}{\Gamma_d}\left(\frac{dT_0}{dt} - \frac{dT_{\mathrm{LCL}}}{dt}\right). \tag{9}$$

The rate of change of surface temperature T_0 is implied by the energy balance (6). The temperature at z_b is T_{LCL}, defined as

$$q_t = q_s(T_{\mathrm{LCL}}).$$

We can take the time derivative and use the chain rule to get the time rate of change of T_{LCL},

$$\frac{dT_{\mathrm{LCL}}}{dt} = \frac{dq_t}{dt}\left(\frac{dq_s}{dT}\Big|_{T_{\mathrm{LCL}}}\right)^{-1}. \tag{10}$$

By plugging in (10) into (9) and using (6), (7), and (8), we find

$$\frac{dz_b}{dt} = \frac{1}{\Gamma_d z_i}\left[a_2 B - w_e \Delta q_t \left(\frac{dq_s}{dT}\Big|_{T_{\mathrm{LCL}}}\right)^{-1}\right].$$

Next, we subtract the equation for the cloud base from the mass balance (5) to get the time tendency equation for cloud thickness,

$$\frac{d\Delta z_{\mathrm{cloud}}}{dt} = w_e\left[1 + \frac{\Delta q_t}{\Gamma_d z_i}\left(\frac{dq_s}{dT}\Big|_{T_{\mathrm{LCL}}}\right)^{-1}\right] - \frac{a_2 B}{\Gamma_d z_i} + w_{LS}. \tag{11}$$

Now we can use (11) to understand how $\Delta z_{\mathrm{cloud}}$ responds to idealized climate changes:

- Cases with different $\theta_{l,0}$ have different initial z_b. The warmest cases start with the lowest cloud bases and thus with the thickest clouds, as a result of fixing the relative humidity at the surface. Despite an increase of dz_b/dt with $\theta_{l,0}$, $\Delta z_{\mathrm{cloud}}$ at the end still shows a decrease with $\theta_{l,0}$ because the rate of change is not high enough to overcome the initial z_b differences in 12 hours of simulations (see the Appendix for more discussion).
- Cloud thickness decreases with inversion strength $\Delta\theta_l$ because w_e decreases with $\Delta\theta_l$. Increases in Δq_t with $\Delta\theta_l$ are partially compensated by the increase of dq_s/dT, leaving w_e changes to dominate the changes in the first term on the right-hand side of (11).
- As $\mathcal{H}_f$ increases, $\Delta z_{\mathrm{cloud}}$ increases because Δq_t increases (Δq_t is negative in most cases). The entrainment rate w_e is rather insensitive to changes in $\mathcal{H}_f$. The cloud top height remains constant while the cloud base decreases as more moisture is entrained from the cloud top.

Despite the thinning of the cloud with $\theta_{l,0}$, LWP still increases (Figure 10c). This is because of the changes in the adiabatic liquid water lapse rate Γ_l, defined as

$$\Gamma_l \equiv \frac{dq_l}{dz} = -\frac{dq_s}{dz}.$$

For a saturated cloud layer, the moist static energy is conserved if hydrostaticity is assumed. Therefore,

$$c_p dT + g dz + L_v dq_s = 0,$$

which we can re-write to get

$$\frac{dq_s}{dz} = -\frac{c_p}{L_v}\left(\frac{g}{cp} + \frac{dT}{dz}\right),$$
$$\Gamma_l = \frac{c_p}{L_v}\left(\Gamma_d - \Gamma_m\right).$$

The liquid water lapse rate is a function of temperature and pressure, which is shown in Figure 13. It increases strongly with temperature, and it decreases weakly with pressure, accounting for the increase in LWP with $\theta_{l,0}$.

For each panel in Figure 11, LWP decreases going to the right because cloud thickness $\Delta z_{\mathrm{cloud}}$ decreases with stronger inversions. LWP increases going upward across each panel because the liquid water lapse rate Γ_l increases with temperature. Moving from Figure 11a to d, LWP also increases as $\Delta z_{\mathrm{cloud}}$ thickens with $\mathcal{H}_f$.

Figure 12 shows LWP stratified for constant $\mathcal{H}_f$ in LES. The LES cloud layers are close to adiabatic, although decoupled cases tend to be more sub-adiabatic. This is represented by

the contours with negative slopes in the hatched region on Figure 12d. Adiabatic liquid profiles are calculated using z_b, q_t, and θ_l, assuming the latter two are constant with height up to the cloud top. An adiabatic version of the LWP distribution in the $\Delta\theta_l$-q_t^+ space is comparable to Figure 7b (not shown). The sensitivities of LWP are quantitatively similar to Figure 11, so we expect the same mechanism discussed for the MLM to hold for the LES. The largest discrepancy occurs in Figure 12d. This is expected given that a sizeable portion of the parameter space in this panel shows decoupling.

5.4 Decoupling and Microphysics

A complication to the analysis of the LES is the presence of decoupling in warm and moist conditions. This decoupling is closely tied to precipitation (snow in most cases), which transports water from the cloud layer to the sub-cloud layer [*Solomon et al.*, 2014]. As a result, the cloud layer becomes sub-adiabatic and deviates from the MLM representation. The microphysical processes also have an impact on the stability of the BL: it becomes less stable when the microphysics scheme is turned off (all condensate falls out immediately), especially in simulations with high $\mathcal{H}_f$ (Figure 14a). Without microphysics, the cloud layer is significantly moister than the sub-cloud layer, while the opposite is true with microphysics (Figure 14b).

Savre et al. [2014] also found decoupling when they increased the water vapor content aloft. However, their simulations include a moist surface layer, which provides a major source of moisture for the cloud layer. When this source is absent, as is the case in our ISDAC_i simulations, the importance of ice sublimation becomes evident. We found a stronger cooling in the sub-cloud layer due to sublimation of snow, and stronger warming due to precipitation formation with increasing $\mathcal{H}_f$.

6 Summary and Conclusion

To improve our understanding of the sensitivity of Arctic low clouds to climate change, we simulated mixed-phase stratocumulus using the recently developed LES code PyCLES. The setup was based on the ISDAC LES intercomparison project, and the simulated BL agrees reasonably well with aircraft observations. Subsequently, we conducted sensitivity experiments in a modified ISDAC setup.

By varying parameters that control the initial BL structure, such as temperature, inversion strength at cloud top, and free-tropospheric relative humidity, we explored the BL response to different climates in an idealized setting. We showed that Arctic stratocumulus can be represented well with a MLM, as long as the BL does not become strongly decoupled. Most cases studied here have a cloud layer dominated by liquid close to adiabatic amounts, despite an increase of sub-adiabaticity in cases with high free-tropospheric relative humidity.

The adiabatic LWP increases with BL temperature and free-tropospheric relative humidity, and it decreases with inversion strength. This can be understood in the MLM framework through the dependence of the liquid water lapse rate and cloud thickness on the three parameters. Most of the LES have similar parameter dependencies as those exposed by the MLM, except for cases with decoupled BL. Decoupling arises when microphysical processes transport moisture from the cloud layer to the sub-cloud layer.

The three parameters we chose to vary have implications for Arctic climate change. For example, surface amplified warming is likely to reduce the inversion strength capping the BL. When this occurs over sea ice, where surface fluxes are weak, we expect LWP to increase based on our experiments. If a decrease of free-tropospheric relative humidity accompanies warming in the Arctic, it would imply a decreased LWP sensitivity to inversion strength, but an increased sensitivity to BL temperature (Figure 11).

The simplified ISDAC_i setup has its limitations. For example, we have not tested the sensitivities of the BL and clouds to surface fluxes. As sea ice extent continues to decline in the Arctic Ocean, surface heat fluxes will become more important in driving BL turbulence. A next step is to investigate how such surface flux changes and other changes in the large-scale circulation can affect Arctic low cloud cover more broadly.

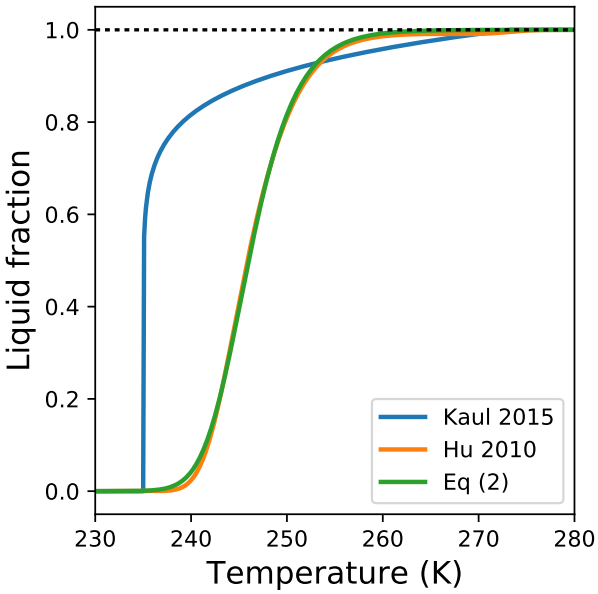

482 **Figure 1.** Liquid fraction as a function of temperature.

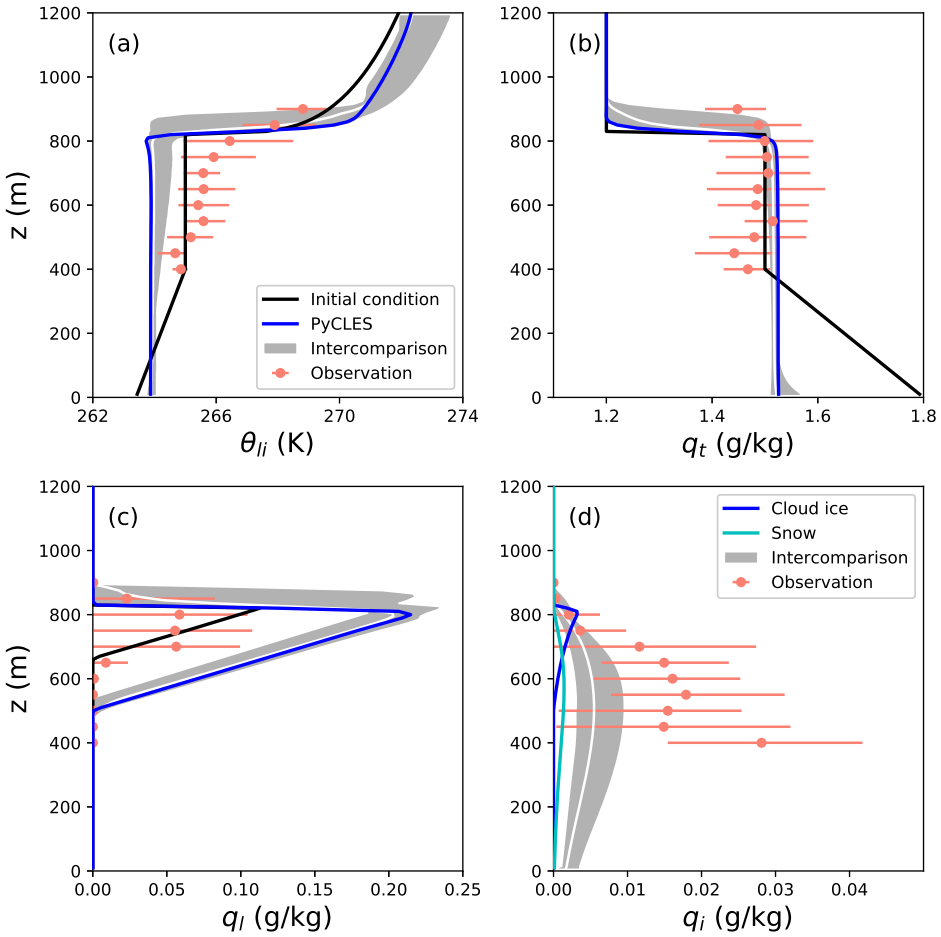

Figure 2. Domain mean profiles of (a) liquid ice potential temperature, (b) total water specific humidity, (c) cloud liquid water specific humidity, and (d) cloud ice and snow water specific humidity. Black lines in (a) and (b) are the initial conditions. Grey shading shows the LES intercomparison range in *Ovchinnikov et al.* [2014], with the white line indicating the ensemble mean profiles. The pink dots show the aircraft observations of Flight 31 of ISDAC campaign on April 27, 2008. The horizontal lines indicate the 15-85 percentile range for the measurements binned for every 50 m.

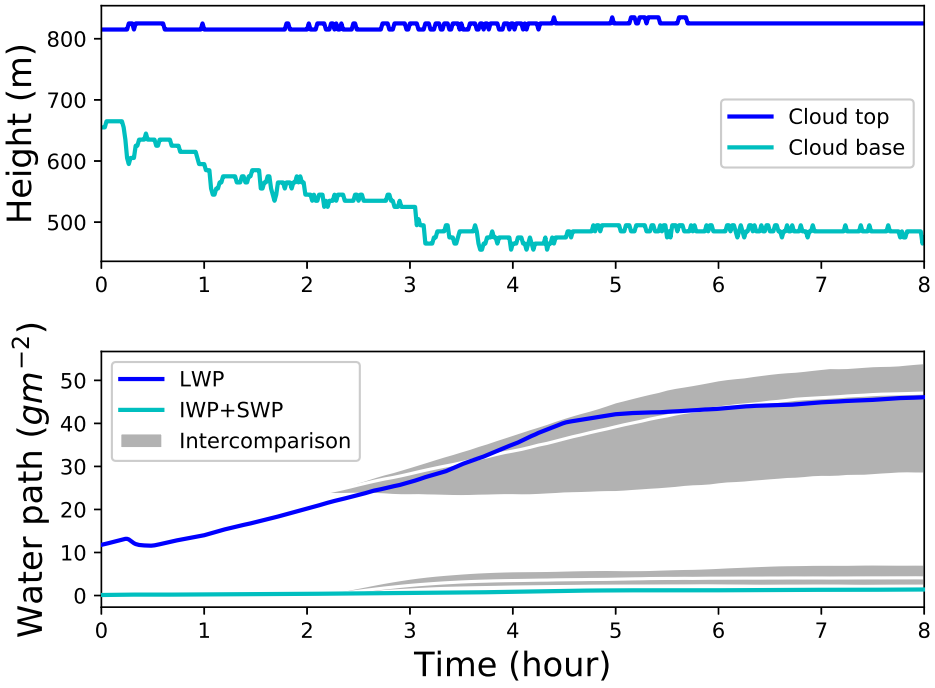

Figure 3. Timeseries of (top) cloud top and base height, and (bottom) liquid and ice water paths. Grey shading shows the LES intercomparison range in *Ovchinnikov et al.* [2014], with the white line indicating the ensemble mean.

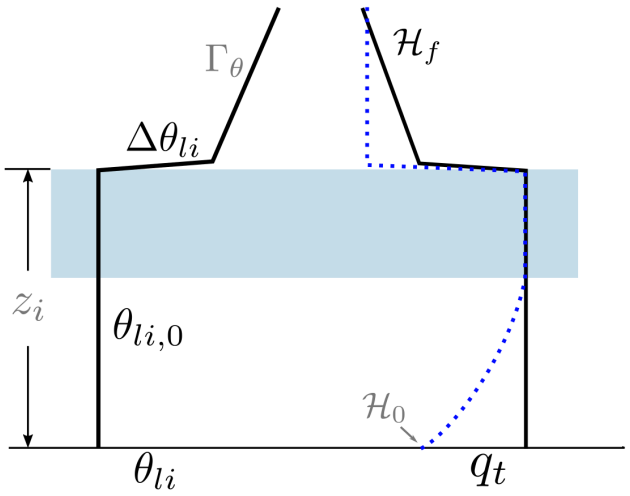

Figure 4. Schematic of the ISDAC_i θ_{li} and q_t initial conditions. The cloud layer is indicated in blue. The BL with height z_i has constant θ_{li} and q_t, where q_t is determined by the relative humidity (blue dotted line) near the surface $\mathcal{H}_0$. Relative humidity above the BL $\mathcal{H}_f$ does not vary with height.

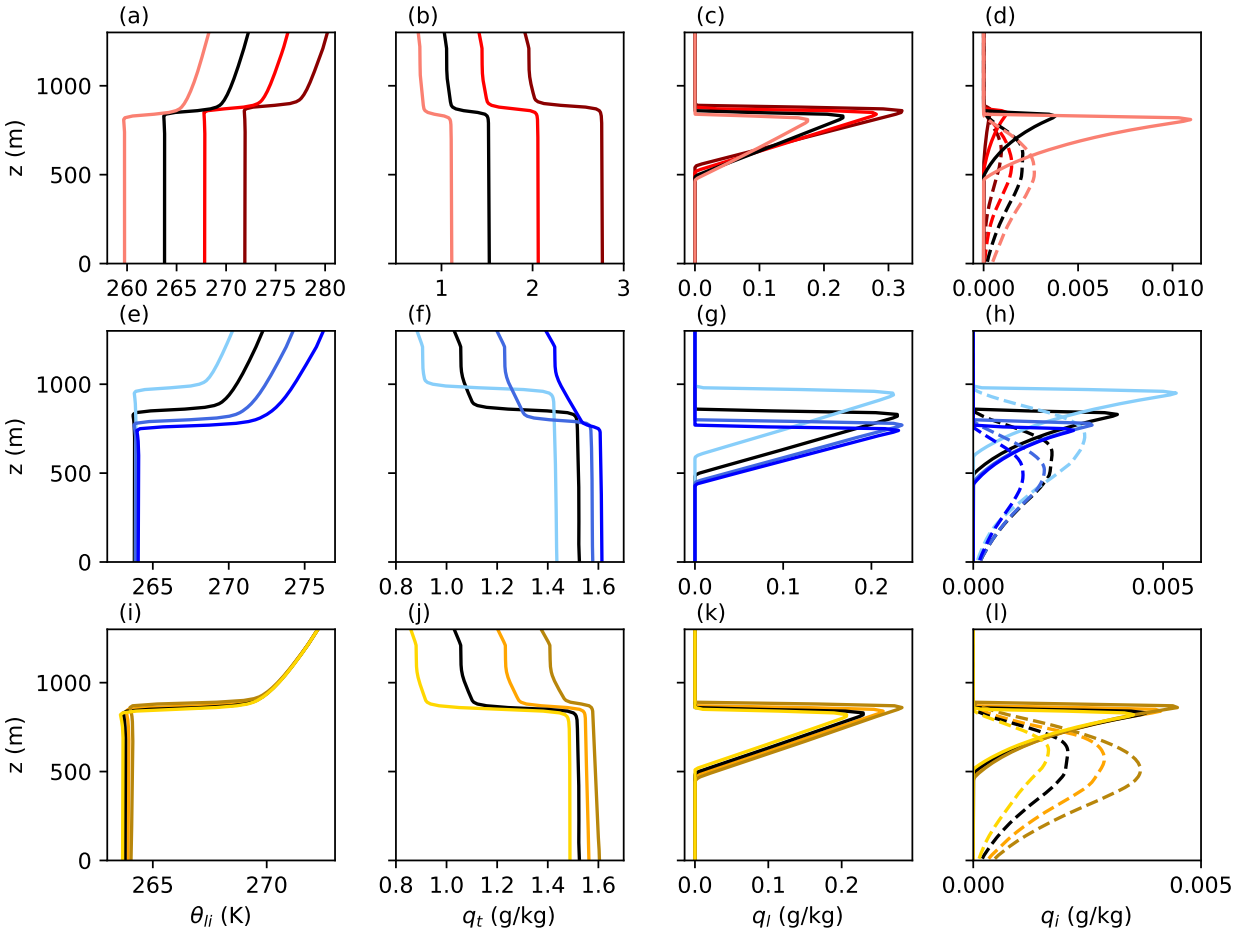

Figure 5. ISDAC_i domain mean profiles of (a, e, i) liquid ice potential temperature, (b, f, j) total water specific humidity, (c, g, k) liquid water specific humidity, and (d, h, l) cloud ice (solid) and snow (dashed) water specific humidity. (a)–(d) Only $\theta_{li,0}$ is varied; (f)–(h) only $\Delta\theta_l$ is varied; (i)-(l) only $\mathcal{H}_f$ is varied. Black profiles show the baseline simulation. Color shadings increase with the parameter values in Table 2.

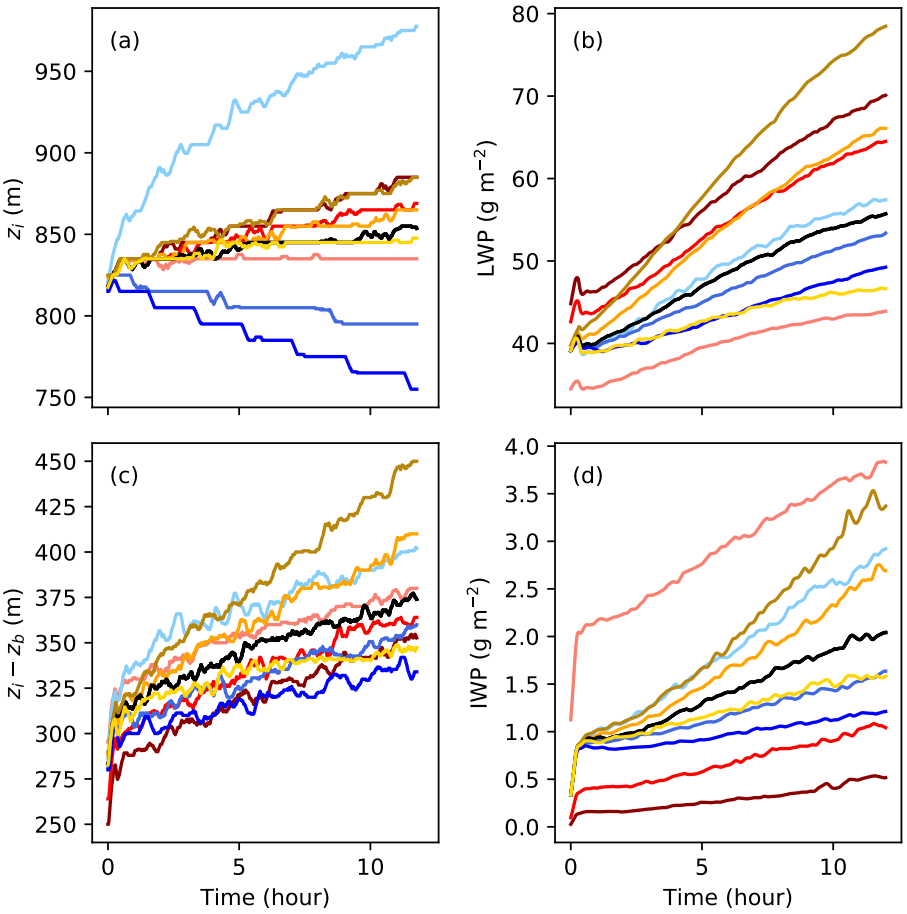

Figure 6. ISDAC_i timeseries of (a) cloud top height, (b) liquid water path, (c) cloud thickness, and (d) ice water path (solid) and snow water path (dashed). Colors as in Figure 5. Cloud top height and cloud thickness are smoothed over 15-minute periods for better visualization.

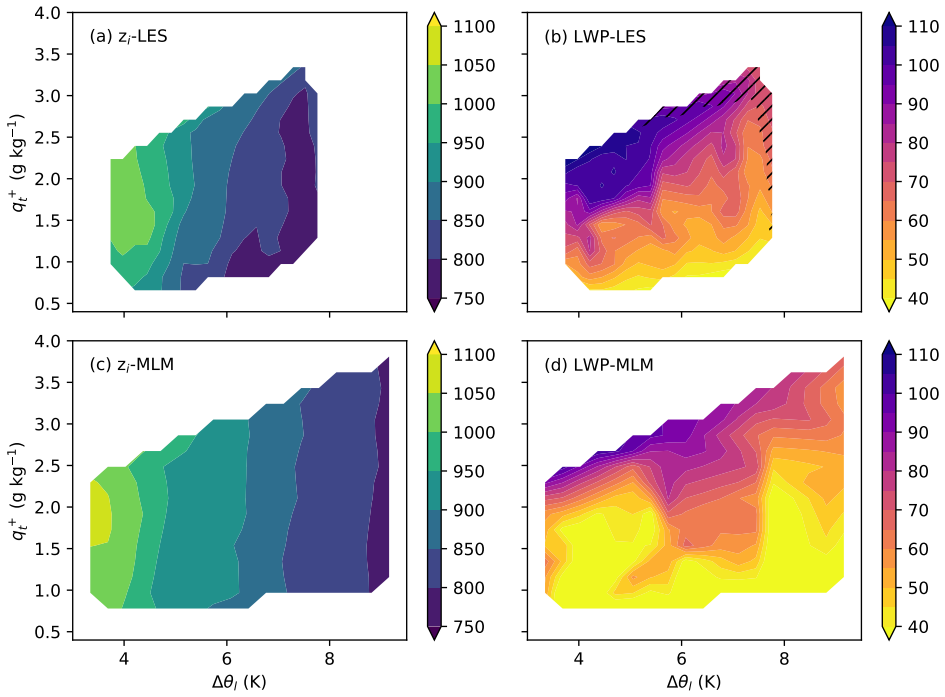

Figure 7. Cloud top height (z_i, in m) and liquid water path (LWP, in g m^{-2}) in climate change simulations with LES (a, b) and with MLM (c, d) averaged at the 12th hour. The horizontal axis shows the inversion strength, and the vertical axis shows the specific humidity right above the cloud top. Hatched regions indicate regions of parameter space where the LES BL decouples, as determined by BIR > 0.15.

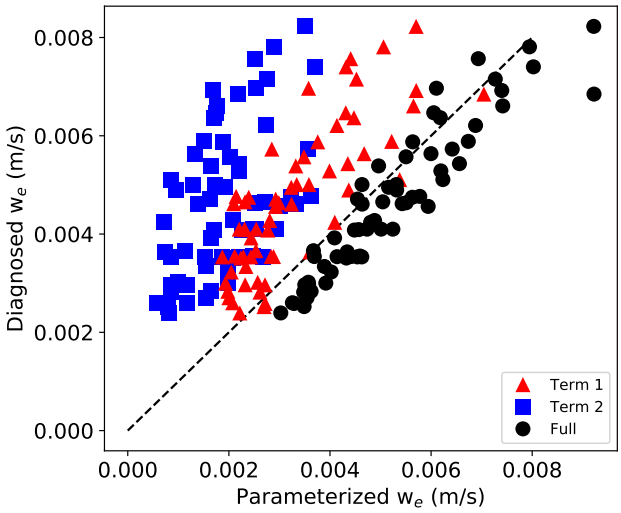

Figure 8. Entrainment rate diagnosed from LES and parameterized using Eq. (8). Term 1 and 2 correspond to the right-hand sides of Eq. (8). The BL-mean buoyancy flux $B = 6.34 \times 10^{-3}$ is fixed for all cases. Term 1 uses $a_2 = 2.0$. The full right-hand side is fitted linearly to the diagnosed entrainment rates with a slope of 0.97 ($R^2 = 0.87$). Intercepts of the linear regressions are assumed zero.

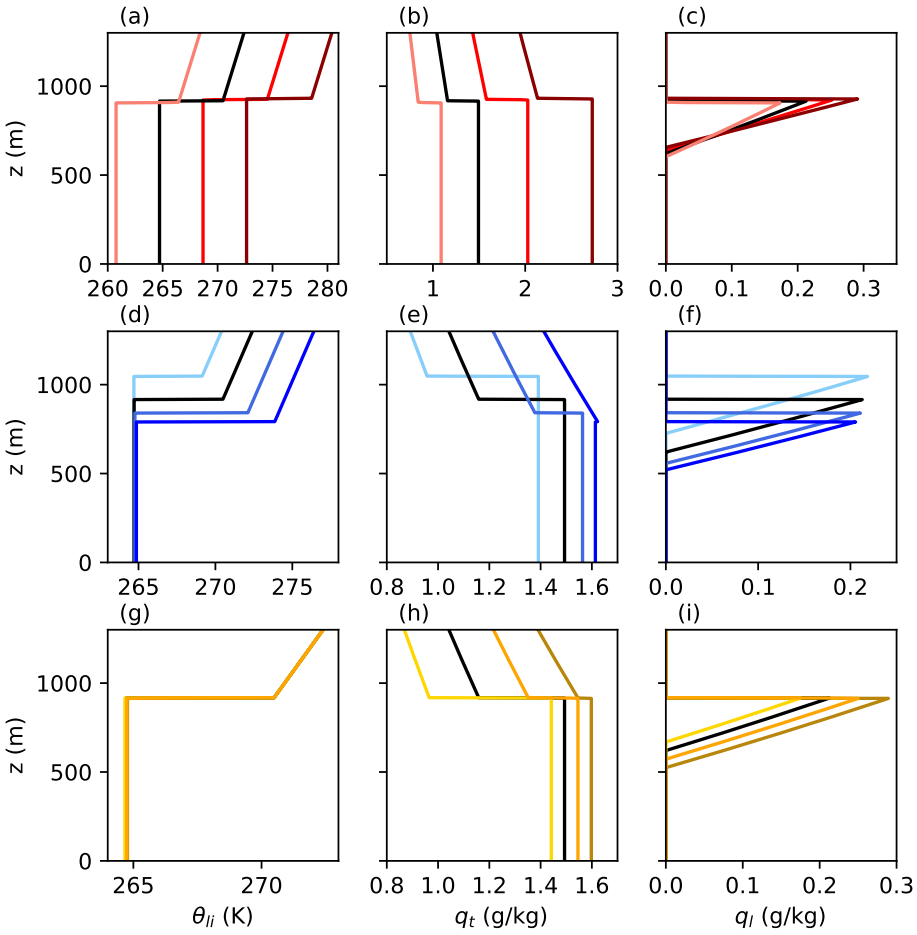

Figure 9. MLM simulations of ISDAC_i domain mean profiles of (a, d, g) liquid ice potential temperature, (b, e, h) total water specific humidity, and (c, f, i) liquid (solid) and ice (dashed) water specific humidity on log scale. (a)–(c) Only $\theta_{li,0}$ is varied; (d)–(f) only $\Delta\theta_l$ is varied; (g)–(i) only $\mathcal{H}_f$ is varied. Colors as in Figure 5.

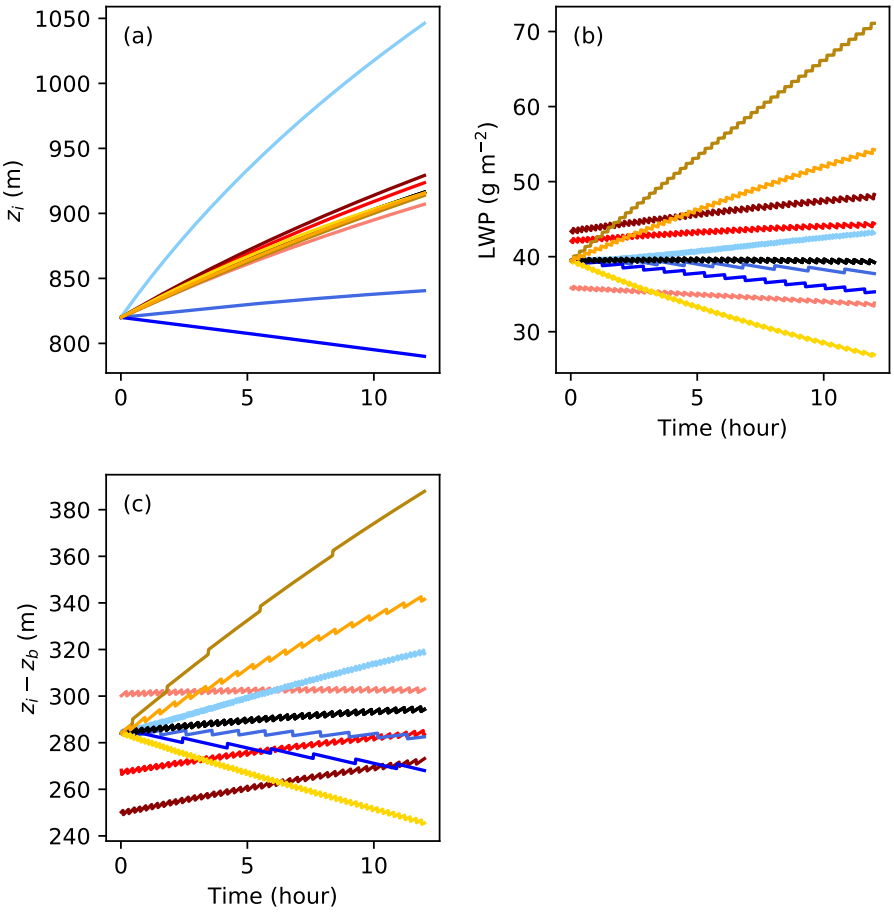

514 **Figure 10.** MLM simulations of ISDAC_i timeseries of (a) cloud top height, (b) liquid water path, and (c)
515 cloud thickness. Colors as in Figure 5.

A: Time tendency of cloud thickness

We checked the correlation between z_i, z_b, and $\Delta z_{\mathrm{cloud}}$ at the end of the simulation (averaged over the 12th hour) and their time tendencies (Figure A.1). The time tendencies are defined as the changes over the last 4 hours of the simulation. We see a very strong positive correlation for z_i across all cases. This is expected given that all simulations start with the same initial z_i. However, this is not the case for z_b, whose initial value varies with temperature. This leads to negative correlations between $\Delta z_{\mathrm{cloud}}$ and $d\Delta z_{\mathrm{cloud}}/dt$ when θ_l is varied while other parameters are held fixed (Figure A.1 bottom, compare markers with same sizes and symbols but different colors). For example, if we compare the largest triangles, the warmest case (red) has the highest $d\Delta z_{\mathrm{cloud}}/dt$ but the thinnest cloud. This is because this case starts with the highest cloud base and thus with the thinnest cloud, which thickens over time. Nevertheless, this effect is largely compensated by the change of liquid water lapse rate, which dominates the sensitivity of LWP to temperature.

Therefore, we can use the correlation between $\Delta z_{\mathrm{cloud}}$ and $d\Delta z_{\mathrm{cloud}}/dt$ to infer the sensitivity of $\Delta z_{\mathrm{cloud}}$ to $\Delta\theta_l$ and $\mathcal{H}_f$, using $d\Delta z_{\mathrm{cloud}}/dt$ derived from MLM.

Acknowledgments

The initial phases of this work were supported by the U.S. National Science Foundation Grants CCF 1048575. We would like to thank Mikhail Ovchinnikov for providing the ISDAC LES intercomparison results. The ISDAC aircraft data were obtained from the Atmospheric Radiation Measurement (ARM) program archive, sponsored by the United States Department of Energy (DOE), Office of Science, Biological and Environmental Research (BER), Environmental Sciences Devision. The PyCLES code is freely available at www.climate-dynamics.org. LES and MLM data are available from the corresponding author upon request.

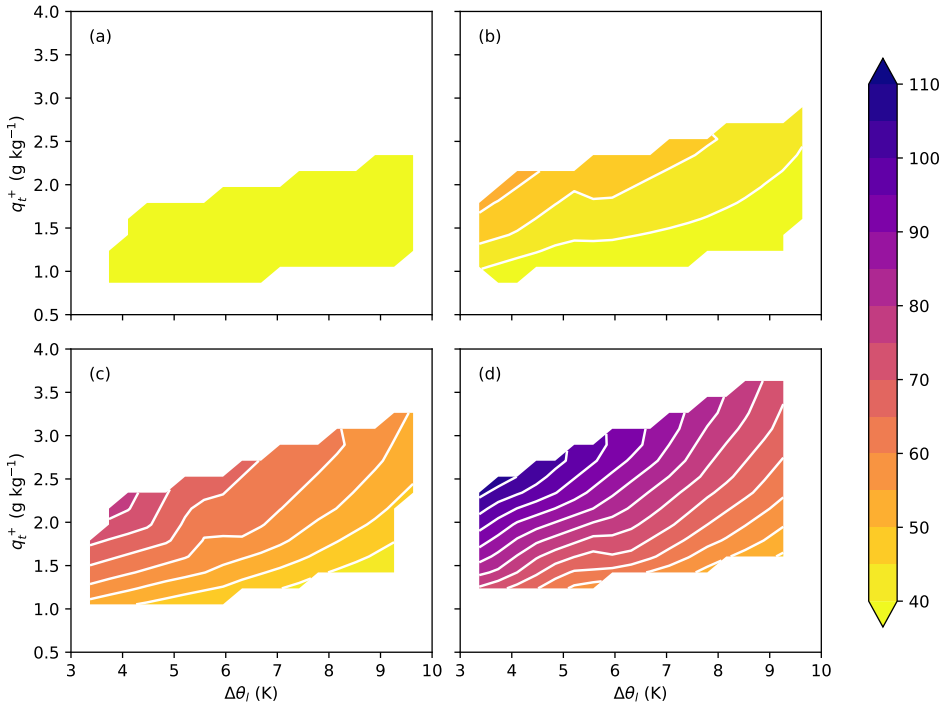

Figure 11. LWP (g m^{-2}) of climate change simulations in MLM with free-tropospheric relative humidity of (a) 50%, (b) 60%, (c) 70%, and (d) 80% at the 12th hour. The horizontal axis shows the inversion strength, and the vertical axis the specific humidity right above the cloud top. The contour interval is 5 g m^{-2}.

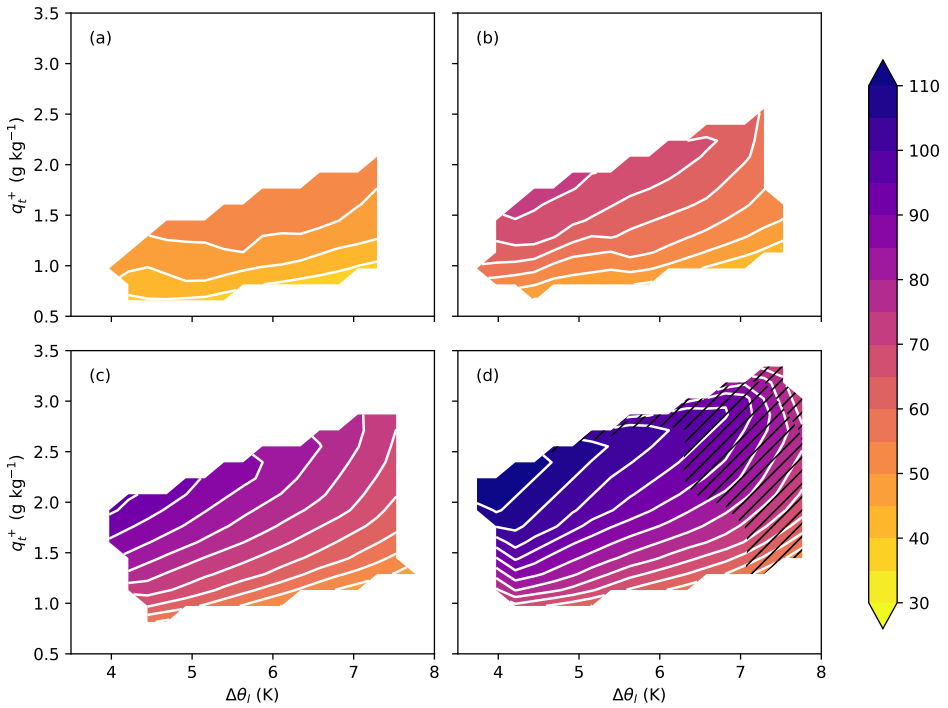

519 **Figure 12.** LWP (g m^{-2}) of climate change LES with free-tropospheric relative humidity of (a) 50%, (b)
520 60%, (c) 70%, and (d) 80% at the 12th hour. The horizontal axis shows the inversion strength, and the ver-
521 tical axis the specific humidity right above the cloud top. The contour interval is 5 g m^{-2}. Hatched regions
522 indicate BIR > 0.15.

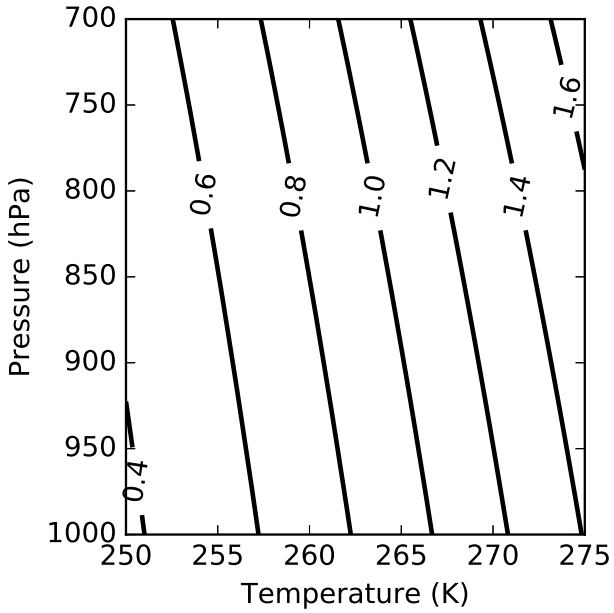

523 **Figure 13.** Liquid water lapse rate Γ_l (g kg^{-1} km^{-1}) as a function of temperature and pressure.

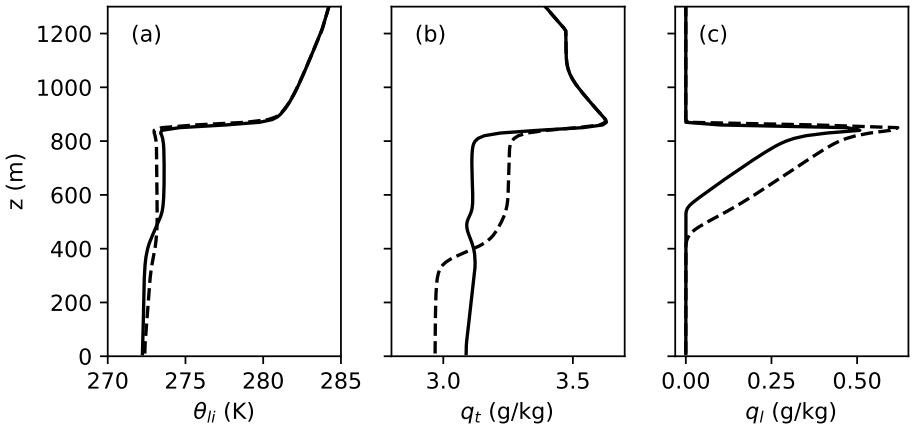

Figure 14. LES profiles of (a) liquid-ice potential temperature, (b) total water specific humidity, and (c) liquid water specific humidity. The case shown here has $\theta_{li,0}$ = 273 K, $\Delta\theta_l$ = 9 K, $\mathcal{H}_f$ = 80%. The solid lines show results with microphysics, and the dashed lines show without microphysics (immediate fallout). Profiles are averaged over the last hour of the simulations.

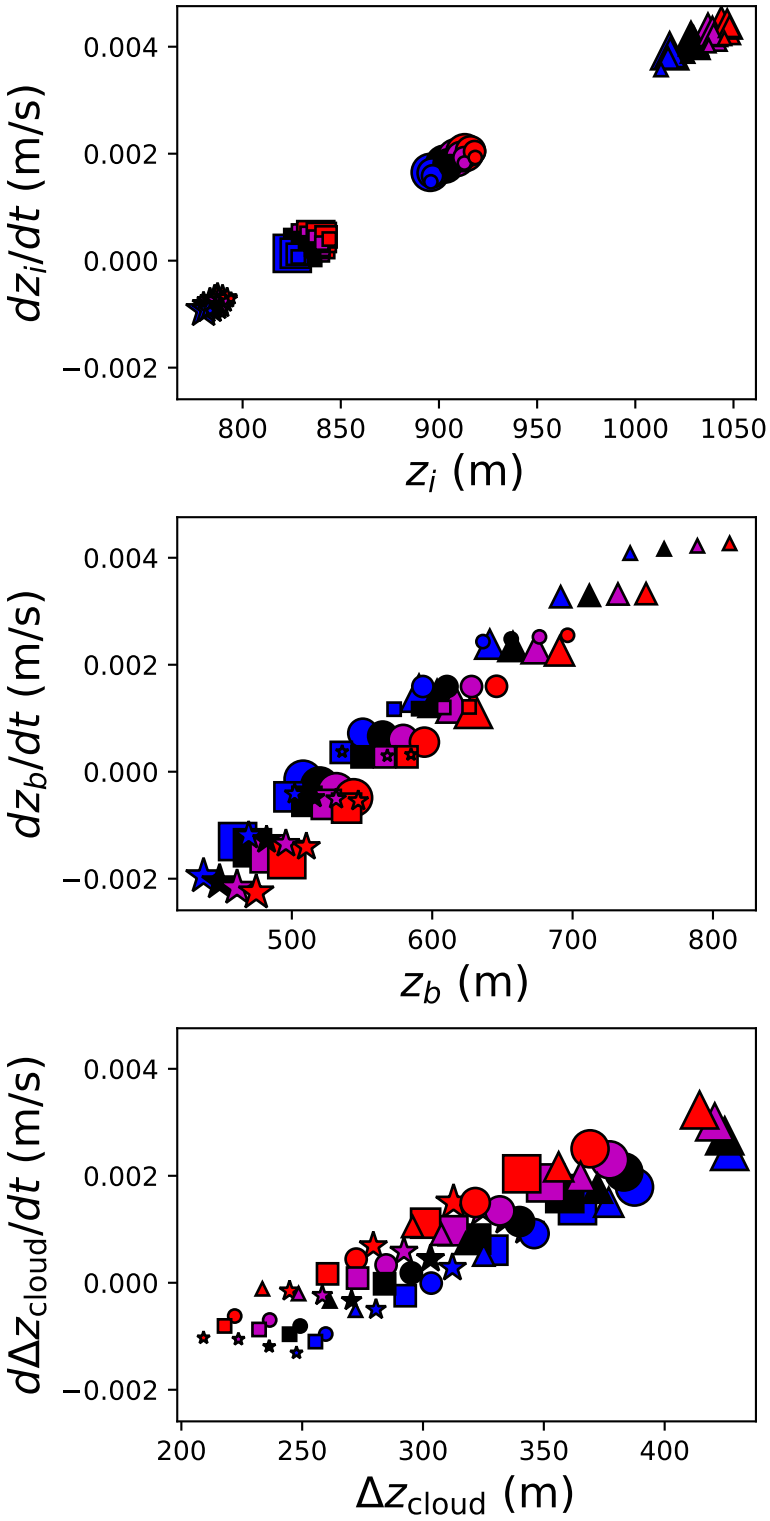

Figure A.1. Scatter plots of (top) cloud top height, (middle) cloud base height, and (bottom) cloud thickness at the end of simulations versus their time tendencies in MLM. Each symbol represents one case. Colors indicate $\theta_{l,0}$: 261 K (blue), 265 K (black), 269 K (magenta), and 273 K (red). Symbol shapes indicate $\Delta\theta_l$: 3 K (triangle), 5 K (circle), 7 K (square), and 9 K (star). Marker sizes from small to large indicate $\mathcal{H}_f = 50\%$, 60%, 70%, and 80%.

References

Blossey, P. N., C. S. Bretherton, M. Zhang, A. Cheng, S. Endo, T. Heus, Y. Liu, A. P. Lock, S. R. de Roode, and K.-M. Xu (2013), Marine low cloud sensitivity to an idealized climate change: The CGILS LES intercomparison, *Journal of Advances in Modeling Earth Systems*, *5*(2), 234–258, doi:10.1002/jame.20025.

Boudala, F. S., G. A. Isaac, Q. Fu, and S. G. Cober (2002), Parameterization of effective ice particle size for high-latitude clouds, *International Journal of Climatology*, *22*(10), 1267–1284, doi:10.1002/joc.774.

Bretherton, C. S., and M. C. Wyant (1997), Moisture transport, lower-tropospheric stability, and decoupling of cloud-topped boundary layers, *Journal of the Atmospheric Sciences*, *54*(1), 148–167, doi:10.1175/1520-0469(1997)054<0148:MTLTSA>2.0.CO;2.

Cox, C. J., T. Uttal, C. N. Long, M. D. Shupe, R. S. Stone, and S. Starkweather (2016), The role of springtime Arctic clouds in determining autumn sea ice extent, *Journal of Climate*, *29*(18), 6581–6596, doi:10.1175/JCLI-D-16-0136.1.

de Boer, G., E. W. Eloranta, and M. D. Shupe (2009), Arctic mixed-phase stratiform cloud properties from multiple years of surface-based measurements at two high-latitude locations, *Journal of the Atmospheric Sciences*, *66*(9), 2874–2887, doi:10.1175/2009JAS3029.1.

De Roode, S. R., A. P. Siebesma, S. D. Gesso, H. J. J. Jonker, J. Schalkwijk, and J. Sival (2014), A mixed-layer model study of the stratocumulus response to changes in large-scale conditions, *Journal of Advances in Modeling Earth Systems*, *6*(4), 1256–1270, doi:10.1002/2014MS000347.

Gesso, S. D., A. P. Siebesma, S. R. de Roode, and J. M. van Wessem (2014), A mixed-layer model perspective on stratocumulus steady states in a perturbed climate, *Quarterly Journal of the Royal Meteorological Society*, *140*(684), 2119–2131, doi:10.1002/qj.2282.

Grabowski, W. W. (1998), Toward cloud resolving modeling of large-scale tropical circulations: A simple cloud microphysics parameterization, *Journal of the Atmospheric Sciences*, *55*(21), 3283–3298, doi:10.1175/1520-0469(1998)055<3283:TCRMOL>2.0.CO;2.

Graversen, R. G., and M. Wang (2009), Polar amplification in a coupled climate model with locked albedo, *Climate Dynamics*, *33*(5), 629–643, doi:10.1007/s00382-009-0535-6.

Holland, M. M., and C. M. Bitz (2003), Polar amplification of climate change in coupled models, *Climate Dynamics*, *21*(3), 221–232, doi:10.1007/s00382-003-0332-6.

Hu, Y., S. Rodier, K.-m. Xu, W. Sun, J. Huang, B. Lin, P. Zhai, and D. Josset (2010), Occurrence, liquid water content, and fraction of supercooled water clouds from combined CALIOP/IIR/MODIS measurements, *Journal of Geophysical Research: Atmospheres*, *115*(D4), doi:10.1029/2009JD012384, d00H34.

Iacono, M. J., J. S. Delamere, E. J. Mlawer, M. W. Shephard, S. A. Clough, and W. D. Collins (2008), Radiative forcing by long-lived greenhouse gases: Calculations with the AER radiative transfer models, *Journal of Geophysical Research: Atmospheres*, *113*(D13), doi:10.1029/2008JD009944, d13103.

Intrieri, J. M., M. D. Shupe, T. Uttal, and B. J. McCarty (2002), An annual cycle of Arctic cloud characteristics observed by radar and lidar at SHEBA, *Journal of Geophysical Research: Oceans*, *107*(C10), SHE 5–1–SHE 5–15, doi:10.1029/2000JC000423.

Karlsson, J., and G. Svensson (2013), Consequences of poor representation of arctic sea-ice albedo and cloud-radiation interactions in the cmip5 model ensemble, *Geophysical Research Letters*, *40*(16), 4374–4379, doi:10.1002/grl.50768.

Kaul, C. M., J. Teixeira, and K. Suzuki (2015), Sensitivities in large-eddy simulations of mixed-phase Arctic stratocumulus clouds using a simple microphysics approach, *Monthly Weather Review*, *143*(11), 4393–4421, doi:10.1175/MWR-D-14-00319.1.

Kay, J. E., and T. L'Ecuyer (2013), Observational constraints on Arctic ocean clouds and radiative fluxes during the early 21st century, *Journal of Geophysical Research:*

Atmospheres, *118*(13), 7219–7236, doi:10.1002/jgrd.50489.

Kay, J. E., T. L'Ecuyer, H. Chepfer, N. Loeb, A. Morrison, and G. Cesana (2016), Recent advances in Arctic cloud and climate research, *Current Climate Change Reports*, *2*(4), 159–169, doi:10.1007/s40641-016-0051-9.

Lilly, D. K. (1968), Models of cloud-topped mixed layers under a strong inversion, *Quarterly Journal of the Royal Meteorological Society*, *94*(401), 292–309, doi:10.1002/qj.49709440106.

Manabe, S., and R. T. Wetherald (1975), The effects of doubling the CO_2 concentration on the climate of a general circulation model, *Journal of the Atmospheric Sciences*, *32*(1), 3–15, doi:10.1175/1520-0469(1975)032<0003:TEODTC>2.0.CO;2.

Martin, G. M., D. W. Johnson, and A. Spice (1994), The measurement and parameterization of effective radius of droplets in warm stratocumulus clouds, *Journal of the Atmospheric Sciences*, *51*(13), 1823–1842, doi:10.1175/1520-0469(1994)051<1823:TMAPOE>2.0.CO;2.

McFarquhar, G. M., S. Ghan, J. Verlinde, A. Korolev, J. W. Strapp, B. Schmid, J. M. Tomlinson, M. Wolde, S. D. Brooks, D. Cziczo, M. K. Dubey, J. Fan, C. Flynn, I. Gultepe, J. Hubbe, M. K. Gilles, A. Laskin, P. Lawson, W. R. Leaitch, P. Liu, X. Liu, D. Lubin, C. Mazzoleni, A.-M. Macdonald, R. C. Moffet, H. Morrison, M. Ovchinnikov, M. D. Shupe, D. D. Turner, S. Xie, A. Zelenyuk, K. Bae, M. Freer, and A. Glen (2011), Indirect and Semi-direct Aerosol Campaign, *Bulletin of the American Meteorological Society*, *92*(2), 183–201, doi:10.1175/2010BAMS2935.1.

Moeng, C.-H., P. P. Sullivan, and B. Stevens (1999), Including radiative effects in an entrainment rate formula for buoyancy-driven PBLs, *Journal of the Atmospheric Sciences*, *56*(8), 1031–1049, doi:10.1175/1520-0469(1999)056<1031:IREIAE>2.0.CO;2.

Morrison, H., P. Zuidema, G. M. McFarquhar, A. Bansemer, and A. J. Heymsfield (2011), Snow microphysical observations in shallow mixed-phase and deep frontal Arctic cloud systems, *Quarterly Journal of the Royal Meteorological Society*, *137*(659), 1589–1601, doi:10.1002/qj.840.

Ovchinnikov, M., A. S. Ackerman, A. Avramov, A. Cheng, J. Fan, A. M. Fridlind, S. Ghan, J. Harrington, C. Hoose, A. Korolev, G. M. McFarquhar, H. Morrison, M. Paukert, J. Savre, B. J. Shipway, M. D. Shupe, A. Solomon, and K. Sulia (2014), Intercomparison of large-eddy simulations of Arctic mixed-phase clouds: Importance of ice size distribution assumptions, *Journal of Advances in Modeling Earth Systems*, *6*(1), 223–248, doi:10.1002/2013MS000282.

Pressel, K. G., C. M. Kaul, T. Schneider, Z. Tan, and S. Mishra (2015), Large-eddy simulation in an anelastic framework with closed water and entropy balances, *Journal of Advances in Modeling Earth Systems*, doi:10.1002/2015MS000496.

Pressel, K. G., S. Mishra, T. Schneider, C. M. Kaul, and Z. Tan (2017), Numerics and subgrid-scale modeling in large eddy simulations of stratocumulus clouds, *Journal of Advances in Modeling Earth Systems*, doi:10.1002/2016MS000778.

Savre, J., A. M. L. Ekman, and G. Svensson (2014), Technical note: Introduction to MIMICA, a large-eddy simulation solver for cloudy planetary boundary layers, *Journal of Advances in Modeling Earth Systems*, *6*(3), 630–649, doi:10.1002/2013MS000292.

Schneider, T., and I. M. Held (2001), Discriminants of twentieth-century changes in Earth surface temperatures, *J. Climate*, *14*, 249–254.

Serreze, M. C., A. P. Barrett, J. C. Stroeve, D. N. Kindig, and M. M. Holland (2009), The emergence of surface-based arctic amplification, *The Cryosphere*, *3*(1), 11–19, doi:10.5194/tc-3-11-2009.

Serreze, M. C., A. P. Barrett, and J. Stroeve (2012), Recent changes in tropospheric water vapor over the arctic as assessed from radiosondes and atmospheric reanalyses, *Journal of Geophysical Research: Atmospheres*, *117*(D10), doi:10.1029/2011JD017421, d10104.

Sherwood, S. C., W. Ingram, Y. Tsushima, M. Satoh, M. Roberts, P. L. Vidale, and P. A. O'Gorman (2010), Relative humidity changes in a warmer climate, *Journal of Geophysical Research: Atmospheres*, *115*(D9), doi:10.1029/2009JD012585, d09104.

Solomon, A., M. D. Shupe, O. Persson, H. Morrison, T. Yamaguchi, P. M. Caldwell, and G. de Boer (2014), The sensitivity of springtime Arctic mixed-phase stratocumulus clouds to surface-layer and cloud-top inversion-layer moisture sources, *Journal of the Atmospheric Sciences*, *71*(2), 574–595, doi:10.1175/JAS-D-13-0179.1.

Stevens, B. (2006), Bulk boundary-layer concepts for simplified models of tropical dynamics, *Theor. Comput. Fluid Dyn.*, *20*, 279–304, doi:0.1007/s00162-006-0032-z.

Straka, J. (2009), *Cloud and Precipitation Microphysics: Principles and Parameterizations*, Cambridge University Press.

Stroeve, J. C., M. C. Serreze, M. M. Holland, J. E. Kay, J. Malanik, and A. P. Barrett (2012), The Arctic's rapidly shrinking sea ice cover: a research synthesis, *Climatic Change*, *110*(3), 1005–1027, doi:10.1007/s10584-011-0101-1.

Tan, Z., T. Schneider, J. Teixeira, and K. G. Pressel (2016), Large-eddy simulation of subtropical cloud-topped boundary layers: 1. a forcing framework with closed surface energy balance, *Journal of Advances in Modeling Earth Systems*, doi:10.1002/2016MS000655.

Tan, Z., T. Schneider, J. Teixeira, and K. G. Pressel (2017), Large-eddy simulation of subtropical cloud-topped boundary layers: 2. cloud response to climate change, *Journal of Advances in Modeling Earth Systems*, doi:10.1002/2016MS000804.

Tjernström, M., and R. G. Graversen (2009), The vertical structure of the lower Arctic troposphere analysed from observations and the ERA-40 reanalysis, *Quarterly Journal of the Royal Meteorological Society*, *135*(639), 431–443, doi:10.1002/qj.380.

Tripoli, G. J., and W. R. Cotton (1981), The use of ice-liquid water potential temperature as a thermodynamic variable in deep atmospheric models, *Monthly Weather Review*, *109*(5), 1094–1102, doi:10.1175/1520-0493(1981)109<1094:TUOLLW>2.0.CO;2.

Turton, J. D., and S. Nicholls (1987), A study of the diurnal variation of stratocumulus using a multiple mixed layer model, *Quarterly Journal of the Royal Meteorological Society*, *113*(477), 969–1009, doi:10.1002/qj.49711347712.

Wang, X., and J. R. Key (2005), Arctic surface, cloud, and radiation properties based on the AVHRR Polar Pathfinder dataset. part II: Recent trends, *Journal of Climate*, *18*(14), 2575–2593, doi:10.1175/JCLI3439.1.

Wetherald, R. T., and S. Manabe (1975), The effects of changing the solar constant on the climate of a general circulation model, *J. Atmos. Sci.*, *32*, 2044–2059.